

Interplanetary Consequences of Coronal Mass Ejection Events occurred during 18–25 June 2015

P.K. Manoharan,¹ D. Maia,² A. Johri,¹ and M.S. Induja¹

¹*Radio Astronomy Centre, National Centre for Radio Astrophysics, Tata Institute of Fundamental Research, Udhagamandalam (Ooty) 643001, India; mano@ncra.tifr.res.in*

²*CICGE, Faculdade de Ciencias da Universidade do Porto, Porto, Portugal*

Abstract. In this paper, we review the preliminary results on the propagation effects and interplanetary consequences of fast and wide coronal mass ejection (CME) events, occurred during 18–25 June 2015, in the Sun-Earth distance range. The interplanetary scintillation (IPS) images reveal that the large-scale structures of CME-driven disturbances filled nearly the entire inner heliosphere with a range of speeds, $\sim 300\text{--}1000\text{ km s}^{-1}$. The comparison of speed data sets, from IPS technique results in the inner heliosphere and *in-situ* measurements at 1 AU, indicates that the drag force imposed by the low-speed wind dominated heliosphere on the propagation of CMEs may not be effective. The arrival of shocks at 1 AU suggests that a shock can be driven in the interplanetary medium by the central part of the moving CME and also by a different part away from its centre. The increased flux of proton at energies $>10\text{ MeV}$ is consistent with the acceleration of particles by the shock ahead of the CME.

1. Introduction – Coronal Mass Ejections during 18–25 June 2015

Coronal mass ejections (CMEs) move outward from the Sun into the solar wind. Understanding the effects of CMEs in the Sun-Earth distance and identification of their interacting shocks at the Earth’s magnetosphere are scientifically important as well as essential for space weather perspectives. Numerous studies, including models, have been made to investigate the propagation of CMEs in the inner heliosphere (e.g., Dryer et al. (2004); Manoharan et al. (2001); Bisi et al. (2010)). In this study, we consider the radial evolution of large CMEs occurred in the current solar cycle.

According to the sunspot observations, the current solar cycle #24 manifests to be a less intense one in comparison with the previous recent cycles (in fact, this is the smallest sunspot cycle since cycle #14, <http://solarscience.msfc.nasa.gov>). In the course of the current cycle, however, several small and large sunspot groups have produced moderately intense flare/CME events. During June 2015, two groups of fairly large flare-active sunspots passed across the visible disk of the Sun: one in the southern hemisphere (AR#2367, with a magnetic classification of $\beta\gamma$) and the other in the northern hemisphere (AR#2371, $\beta\gamma\delta$ classification). In this study, we consider the period, 18–25 June 2015, during which a number of flares/CMEs and their related eruptions from the above active regions propagated through the heliosphere. In particular, five large CMEs were observed from the above active regions. In Table 1, we list the tim-

ings and locations of these five CME events, along with the available speeds of type-II radio bursts. Four of them were fast halo CMEs (i.e., $V_{\text{CME}} > 1000 \text{ km s}^{-1}$) and were associated with M-class flares at AR#2371. The second event in the list originated from AR#2367 at S21W27 and propelled a partial halo CME of width > 150 degrees, at a nominal speed of $\sim 300 \text{ km s}^{-1}$.

Table 1. List of flares, CMEs, and type-II radio bursts[†]

No.	Date (2015)	Flare Class	Flare Loc.	CME Time (UT)	CME Type	CME Speed (km s^{-1})	Type-II Speed (km s^{-1})	Active Region #
1	18 June	M3.0/1N	N15E50	17:24	Halo	~ 1100		2371
2	19 June		S21W27	06:42	PHalo	~ 300		2367
3	21 June	M2.6	N12E13	02:48	Halo	~ 1200	> 700	2371
4	22 June	M6.5	N12W08	18:36	Halo	1250	~ 1400	2371
5	25 June	M7.9/3B	N10W42	08:36	Halo	1500	~ 1700	2371

[†]The solar radio spectral data sets are from US Air Force Radio Solar Telescope Network (RSTN) and are available at ftp://ftp.ngdc.noaa.gov/STP/SOLAR_DATA.

A major geomagnetic storm ($\text{Dst} = -204 \text{ nT}$ for a prolonged period on 23 June 2015; <http://wdc.kugi.kyoto-u.ac.jp>) was caused by the fast CME event on 21 June 2015 (Table 1, event #3), which was associated with an M2.6 flare from AR#2371 at N12E13. The white-light images of the above CME event, obtained from the LASCO C2/C3 coronagraphs Brueckner et al. (1995), are displayed in Figure 1. The fast expanding full halo structure, along with the filament moving in the north-east direction, can evidently be observed in these images. Since the originating location of the CME event was to the east of the central meridian of the Sun, the direction of propagation of the CME (also its expansion) was oriented to the east with respect to the Sun-Earth line. The LASCO images typically cover up to a heliocentric distance of about 30 solar radii (R_{\odot}) ($1 \text{ AU} \approx 215 R_{\odot}$). The interplanetary scintillation (IPS) observations have been employed in tracking the consequences of propagation of CMEs farther into the

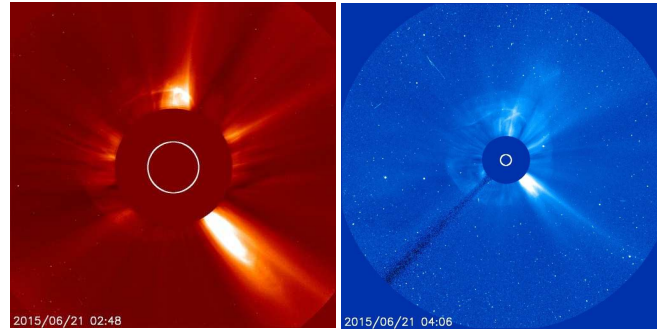


Figure 1. LASCO white-light images of the CME event on 21 June 2015. The *left* and *right* images are, respectively, from C2 and C3 coronagraphs, observed at 02:48 and 04:06 UT. The white circle indicates the limb of the Sun. The colored figure can be found in the electronic version.

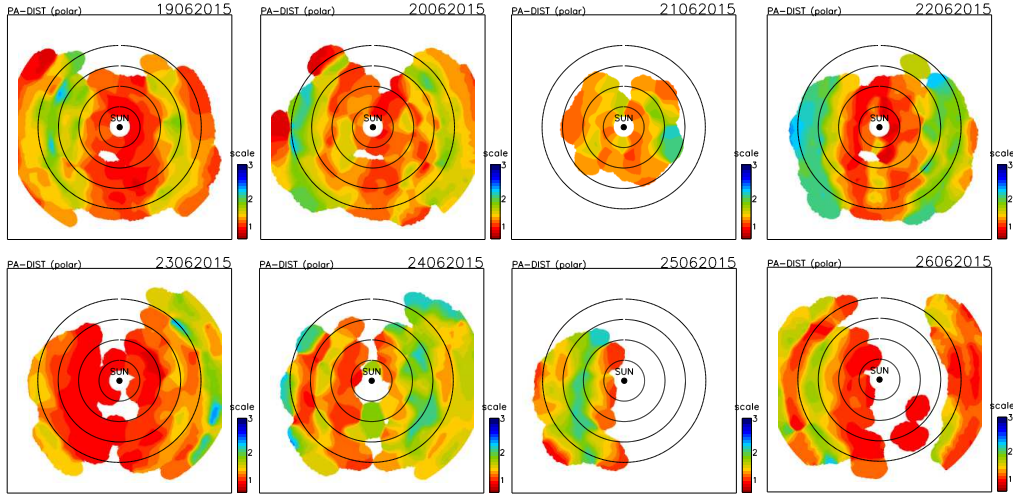


Figure 2. Ooty IPS images for the period 19–26 June 2015. These are similar to the LASCO images and show the sky-plane projection of the inner heliosphere. The concentric circles are of radii, 50, 100, 150, and 200 R_{\odot} . The red color code indicates the background solar wind. In these images, observing time increases from right (west of Sun) to left (east of Sun). The enhanced scintillation regions are the CME-driven disturbances in the IPS field of view. The white patches indicate the data gaps. The colored figure can be found in the electronic version.

inner heliosphere at distances $\geq 50 R_{\odot}$ (e.g., Manoharan et al. (2000); Manoharan et al. (2001)).

1.1. Interplanetary Scintillation Images

The IPS observation from a radio source can provide estimates of solar wind speed and normalized scintillation index (g -index, which is directly related to the level of density turbulence in the solar wind, i.e., ΔN_e) at the closest solar approach of the line of sight to the radio source (e.g., Manoharan (1993); Manoharan et al. (2000)). The IPS measurements at the Ooty Radio Telescope (ORT) on a grid of a large number of radio sources allow to image the disturbances associated with the CMEs at different distances from the Sun before their arrival at the near-Earth space (for details on Ooty IPS studies refer to Manoharan et al. (2000); Manoharan (2010); Bisi et al. (2010)). The images of normalized scintillation index (g -maps) obtained from the Ooty measurements between 19 and 26 June 2015 are displayed in Figure 2. These images are the sky-plane projection of the inner heliosphere, as viewed from the Earth and the vertical (top to bottom) and horizontal (left to right) directions, respectively, represent north-south and east-west directions of the heliosphere. In these images, the observing time increases from right to left (i.e., from west of the Sun to east). Thus, each image shows the three-dimensional distribution of ΔN_e on a given day around the Sun, over a heliospheric diameter of ~ 2 AU. For example, a g -value close to unity, $g \approx 1$, corresponds to the condition of the ambient solar wind and values of $g > 1$ and $g < 1$ represent, respectively, enhancement and depletion in levels of density turbulence (i.e., ΔN_e) in the solar wind. The large-scale structures of enhanced scintillation seen in these images show the presence of CME-associated disturbances in the interplanetary medium. The outward

displacement from the centre of the heliosphere and increase in size of these structures with time suggest the typical speed of propagation and interplanetary consequences of the CMEs.

In this period of study, 18–25 June 2015, the Sun was not dominated by mid-latitude coronal hole(s) and the contribution from the interaction of fast-slow solar wind streams was expected to be insignificant (in general, the effects of such interactions are observed at distances larger than 1 AU (e.g., Gosling (1996))). Therefore, the IPS images shown in Figure 2 reveal the consequences of CMEs related disturbances in the interplanetary medium. On all these days, the inner heliosphere was filled with the CME-associated disturbances of a high level of density turbulence.

2. Speed Distribution of CME-driven Disturbances

Some of the disturbances seen in the IPS images were produced by the fast halo CMEs and they moved with speeds higher than that of the speed of the ambient solar wind. Solar wind speed estimates obtained from Ooty IPS observations between 19 and 27 June 2015 are plotted in Figure 3. These plots include speed data from sources for which the observed g -values are well above the ambient level (i.e., $g \geq 2$) and confirm speeds associated with the CME disturbances. It is to be mentioned that since IPS technique probes different parts of the heliosphere, the above plots would include speed measurements from various parts of the CME-driven disturbances. Moreover, since we are interested in understanding the effects of propagation of the CMEs with distance from the Sun, we compare the speeds of solar wind at two heliocentric distance ranges, respectively, $\leq 125 R_{\odot}$ and $> 125 R_{\odot}$. It is evident in these plots that during the passage of CMEs, the interplanetary medium is filled with a range of speeds, ~ 300 – 1000 km s^{-1} . During this period, as indicated by the IPS observations as well as *in-situ* measurements at 1 AU (refer to Figures 4 and 5), the speed of the ambient (i.e., background) solar wind varies in the range of ~ 275 – 375 km s^{-1} . The drag applied by the background solar wind (i.e., the interaction of the CME with the ambient flow) is proportional to $|V_{\text{CME}} - V_{\text{AMBIENT}}|^2$. Therefore, in the current situation (i.e., low-speed dominated background solar wind) the CMEs would likely be slowed down. However, as seen in the above plots, the evolution of high-speed wind (i.e., $> 500 \text{ km s}^{-1}$) between these two regions of the inner heliosphere (i.e., with respect to the midway between the Sun and Earth) is not significant. A similar speed distribution is observed at both the distance ranges.

2.1. Interplanetary Magnetic Field and Plasma Parameters

It is to be noted that the CMEs seen in the IPS field of view were not earthward directed (Figure 2 and refer to Table 1) and thus the centre part of the CMEs would not have been expected to hit the Earth and cause effects at the near-Earth space. However, in this period of the study, six interplanetary shocks were recorded in the *in-situ* data sets observed at the near-Earth orbit and two geomagnetic storms (i.e., an intense storm, $\text{Dst} = -204 \text{ nT}$ and the other of moderate strength storm, $\text{Dst} = -86 \text{ nT}$) were observed by the geomagnetic observatories. Figure 4 shows the interplanetary plasma and magnetic field parameters of the ambient solar wind and CME-driven shock disturbances observed at 1 AU. These data sets have been obtained from the *OMNIWeb Plus Interface* (<http://omniweb.gsfc.nasa.gov>). Figure 4 shows from top to bottom (i) average magnetic field, $\langle B \rangle$, (ii) solar wind proton speed, V_p , (iii) density, N_p , (iv) proton tem-

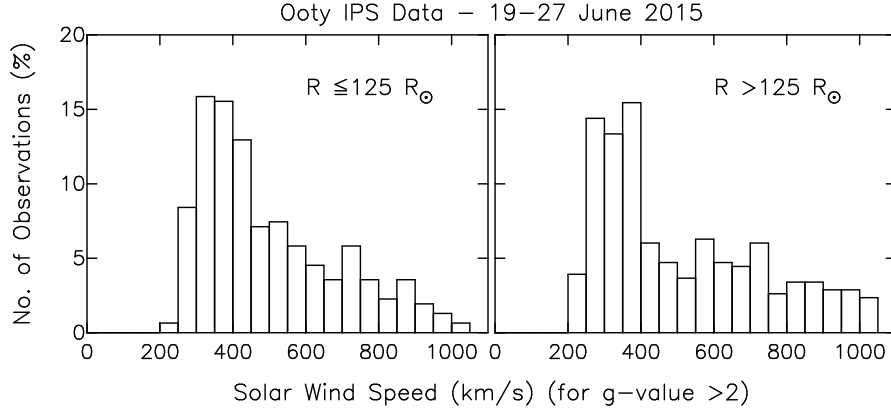


Figure 3. Histograms of solar wind speed estimates obtained from the Ooty IPS measurements at distances, respectively, $\leq 125 R_{\odot}$ (left plot) and $> 125 R_{\odot}$ (right plot). The y-axis marks the percentage of number of observations in each speed bin normalized by the total number of observations considered. These plots include speed data from sources for which the measured g-values are ≥ 2 and this criterion would allow only the enhanced level of scintillation caused by the propagating CME disturbances to be taken into account.

perature, T_p , and (v) proton flux at energy > 10 MeV. These plots have been made using 5-min averaged data sets. Figure 4 also includes the plot of hourly Dst value, which denotes the intensity of the geomagnetic storm. This figure illustrates the conditions of the solar wind prior to the shocks (i.e., unshocked ambient solar wind), shocked plasma and the conditions of driver gas associated with the CMEs. The arrival of six shocks are indicated by dashed vertical lines. The CME behind the shock #3 revealed a flux-rope like structure in the plasma and magnetic field data. The proton flux plotted in Figure 4 shows increase in flux between ~ 21 and 28 June 2015. It is likely that the above CME-driven shocks in the Sun-Earth space have supported the acceleration of particles to high energies.

Since the IPS observations allow to probe the properties of the solar wind in three-dimensional space, the preliminary results of Ooty IPS tomographic reconstruction suggest that (i) CME events #3 and #4 were nearly Earth directed and the earlier one caused an intense shock as well as a major storm of intensity $Dst = -204$ nT at the Earth (refer to shock #3 in Figure 4); (ii) for other events listed in Table 1, only the tail part of the CME crossed the Earth (i.e., just a glancing blow at the Earth's magnetosphere) and caused shocks of considerable strength, but not the intense storms. The reconstruction also shows that some of the CMEs move intact and retain their loop-like shape even at large solar distances, suggesting that the magnetic energy associated with a CME is important in determining its radial evolution. Given the limitation of space in this book, a detailed paper on the study of IPS tomographic reconstruction of these CME events will be published elsewhere.

In Figure 4, it is to be noted that during 22–26 June 2015 (i.e., day numbers 173 to 178), the solar wind speed at 1 AU remains at a high level, which is well above the ambient speed. When we examine the speed distribution, obtained from the *in-situ* data at 1 AU, it shows that a significant fraction of data points is in the high speed range > 500 km s^{-1} . Figure 5 (left panel) shows the histogram of solar wind speed data obtained from the *in-situ* measurements for the period 19–27 June 2015. It is to be mentioned

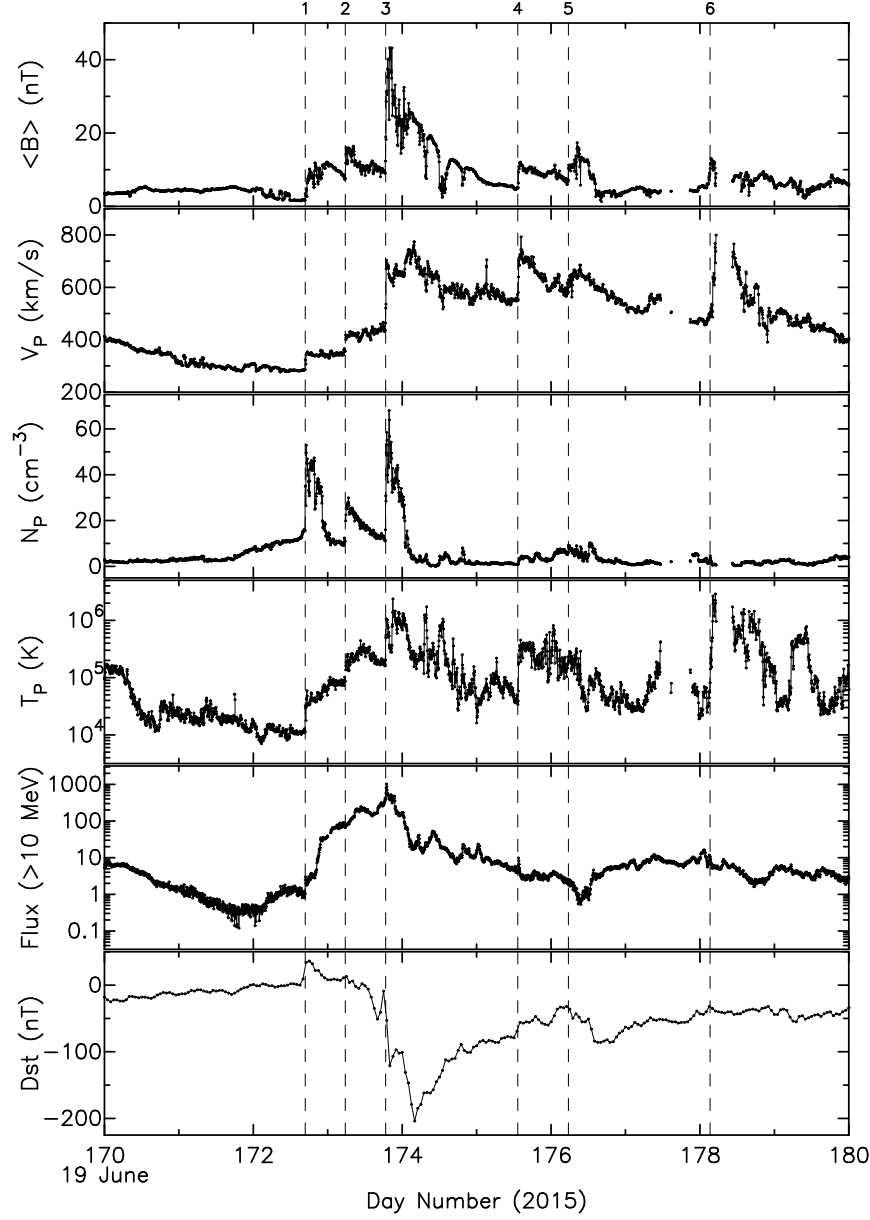


Figure 4. Interplanetary magnetic field and plasma parameters for days 170 to 180 (19–28 June 2015). The geomagnetic index, Dst value, is plotted in the bottom panel of the figure. The Dst index is hourly averaged data and other data sets are from 5-min resolution measurements. The vertical dotted lines indicate the arrival times of shocks and shock numbers are shown at the top.

that this plot includes speeds from the ambient solar wind and CME-associated disturbances. Since not all CME-driven disturbances are Earth directed, this plot includes propagation characteristics of the nearly central part of the CME crossing the Earth as well as the effects of the east or the west wings of the CMEs. As stated earlier, the plots

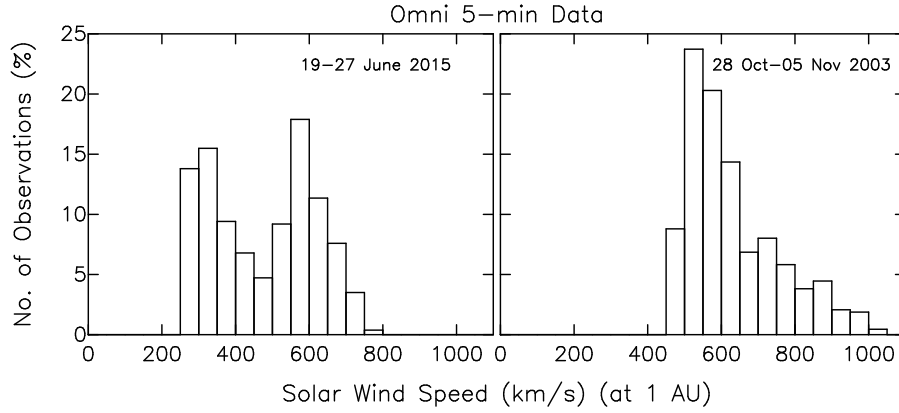


Figure 5. Histograms of *in-situ* solar wind speed obtained from the OMNI database (<http://omniweb.gsfc.nasa.gov/>), for the time periods, respectively, 19–27 June 2015 (*left* plot) and 28 October–05 November 2003 (*right* plot). These plots include ambient solar wind conditions as well as disturbances caused by the CMEs at the near-Earth space.

made from the IPS observations would include speed data from various parts of the propagating CME-driven disturbances. The speed of the ambient (i.e., background) solar wind seems to be low at below 350 km s^{-1} , whereas the speed distribution associated with the CME-driven disturbances lies much above the background flow. At $\sim 1 \text{ AU}$, the drag caused by the ambient solar wind has not been efficient enough to slow down the CME disturbances. It is consistent with the range of speeds obtained from the IPS technique, which gives an overall view of the propagating structures and a significant fraction of them travel at high speeds.

The above inferred solar wind conditions, observed during 19–27 June 2015, have been compared with the largest storm period of the nearly similar phase of the previous cycle, i.e., 28 October – 05 November 2003 (Halloween solar events period). The *right* panel of Figure 5 shows the histogram of solar wind speed data from the *in-situ* measurements. In this plot, the striking feature is that the background solar wind speed is above $\sim 350 \text{ km s}^{-1}$ and is different from the low-speed dominated heliosphere of the current cycle. In spite of the low background speed, in the period 19–27 June 2015, the CME-driven disturbances continue to travel at speeds above 500 km s^{-1} . Whereas in the Halloween period, most of the CMEs originated with rather high speeds (i.e., $\sim 1000\text{--}2000 \text{ km s}^{-1}$) and they significantly evolved in the Sun-Earth distance.

3. Summary

The interplanetary consequences of CME events occurred during 18–25 June 2015 have been analysed based on the white-light images in the near-Sun region, IPS images covering a heliocentric distance range of $50\text{--}200 R_{\odot}$, and *in-situ* measurements at 1 AU . During this period, the inner heliosphere was filled with CME-driven disturbances of a high level of density turbulence (ΔN_e) and their speeds covered a wide range, $\sim 300\text{--}1000 \text{ km s}^{-1}$. Moreover, at this phase of the cycle, the heliosphere was dominated by low-speed ambient flows ($\sim 275\text{--}375 \text{ km s}^{-1}$), which likely did not slow down the CMEs. The solar wind speed distributions at two distances (i.e., $\leq 125 R_{\odot}$ and > 125

R_{\odot}) as well as at 1 AU are consistent with the less radial evolution of speed. The loop-like structures seen in some of the CMEs maintain their shape even at large distances from the Sun and it indicates the importance of magnetic and/or internal energy within a CME in controlling the radial evolution (e.g., Manoharan (2010); Manoharan & Mujiber Rahman (2011)). Since the effective radial evolution can vary from one CME to the other, it is essential that not only the drag effected by the background flows, but also the internal energy of a CME and its rate of dissipation in the interplanetary medium are required to be considered in understanding the radial evolution of the CME.

Acknowledgments. Members of the Radio Astronomy Centre (NCRA-TIFR) are acknowledged for making the ORT available for IPS observations. SOHO/LASCO is a project of international cooperation between ESA and NASA. The near-Earth solar wind data and geomagnetic indexes have been obtained from OMNIWeb service and OMNI data of NASA/GSFC's Space Physics Data Facility (<http://omniweb.gsfc.nasa.gov>). We acknowledge National Geophysical Data Center for the solar data used in this study. This work was partially supported by the CAWSES-India Program, sponsored by ISRO.

References

- Bisi, M. M., Breen, A. R., Jackson, B. V., Fallows, R. A., Walsh, A. P., Mikić, Z., Riley, P., Owen, C. J., Gonzalez-Esparza, A., Aguilar-Rodriguez, E., Morgan, H., Jensen, E. A., Wood, A. G., Owens, M. J., Tokumaru, M., Manoharan, P. K., Chashei, I. V., Giunta, A. S., Linker, J. A., Shishov, V. I., Tyul'Bashev, S. A., Agalya, G., Glubokova, S. K., Hamilton, M. S., Fujiki, K., Hick, P. P., Clover, J. M., & Pintér, B. 2010, *Solar Phys.*, 265, 49
- Brueckner, G. E., Howard, R. A., Koomen, M. J., Korendyke, C. M., Michels, D. J., Moses, J. D., Socker, D. G., Dere, K. P., Lamy, P. L., Llebaria, A., Bout, M. V., Schwenn, R., Simnett, G. M., Bedford, D. K., & Eyles, C. J. 1995, *Solar Phys.*, 162, 357
- Dryer, M., Smith, Z., Fry, C. D., Sun, W., Deehr, C. S., & Akasofu, S.-I. 2004, *Space Weather*, 2, S09001
- Gosling, J. T. 1996, *ARA&A*, 34, 35
- Manoharan, P. K. 1993, *Solar Phys.*, 148, 153
- 2010, *Solar Phys.*, 265, 137
- Manoharan, P. K., Kojima, M., Gopalswamy, N., Kondo, T., & Smith, Z. 2000, *ApJ*, 530, 1061
- Manoharan, P. K., & Mujiber Rahman, A. 2011, *Journal of Atmospheric and Solar-Terrestrial Physics*, 73, 671
- Manoharan, P. K., Tokumaru, M., Pick, M., Subramanian, P., Ipavich, F. M., Schenk, K., Kaiser, M. L., Lepping, R. P., & Vourlidas, A. 2001, *ApJ*, 559, 1180